Saeedian, Meysam; Pouresmaeil, Mobina; Sepehr, Amir; Taheri, Shamsodin; Pouresmaeil, Edris

Small-Signal Stability Analysis of Synthetic Inertia-Based Photovoltaic Generators

Published in:
2021 23rd European Conference on Power Electronics and Applications, EPE 2021 ECCE Europe

Published: 25/10/2021

Document Version
Peer-reviewed accepted author manuscript, also known as Final accepted manuscript or Post-print

Please cite the original version:
Saeedian, M., Pouresmaeil, M., Sepehr, A., Taheri, S., & Pouresmaeil, E. (2021). Small-Signal Stability Analysis of Synthetic Inertia-Based Photovoltaic Generators. In *2021 23rd European Conference on Power Electronics and Applications, EPE 2021 ECCE Europe* IEEE. https://ieeexplore.ieee.org/document/9570644

Small−Signal Stability Analysis of Synthetic Inertia−Based Photovoltaic Generators

Meysam Saeedian[1], Mobina Pouresmaeil[1], Amir Sepehr[1], Shamsodin Taheri[2], and Edris Pouresmaeil[1]
[1]Department of Electrical Engineering and Automation, Aalto University, Espoo, Finland
[2]Department of Computer Science and Engineering, Université du Québec en Outaouais, Gatineau, Canada

Keywords

≪Photovoltaic generator≫, ≪frequency regulation≫, ≪synthetic inertia≫, ≪frequency−locked loop≫.

Abstract

Frequency stability is a consequential issue in power systems dominated by inverter−based generators. To mitigate potential frequency stability problems, inertia emulation concept must be employed in the control of interfaced inverters. This study presents the small−signal state−space realization of a double−stage photovoltaic (PV) generator augmented with synthetic inertia emulator (SIE). The inertia power is provided by the inverter dc−link ultracapacitor. Synchronization of the generator with the host grid is performed using a fast but accurate frequency−locked loop (FLL). The impact of synthetic inertia loop and FLL bandwidth on the PV generator stability is scrutinized as the main contribution. The accuracy of theoretical studies and proper operation of the PV generator are examined through simulations in MATLAB/Simulink.

I. Introduction

Renewable−based energy systems, operating at maximum power point, are widely adopted to reduce greenhouse emission and improve efficiency. Such generators are integrated into the host grid through interfaced power electronic converters, having no rotational inertia and damping properties unlike synchronous generators (SGs) [1]. Diminution of inertia in future power grid challenges the frequency stability assessed with frequency nadir, and rate of change of frequency (RoCoF) [2]. Consequently, the frequency may go beyond the permissible band under severe frequency events, which further may yield under frequency load shedding activation, or cascading collapses [3]. To mitigate the potential frequency stability issues and increase the resilience of low−inertia grids, inertia emulation concept must be employed in the control of interfaced converters [4]; i.e. manipulating the converter power injection to curb the frequency nadir and the RoCoF. Generally, the generation−side inertia emulation mechanisms are categorized as [5]: 1) synchronous condensers, 2) virtual synchronous machines, 3) wind turbines, 4) energy storage systems (batteries, ultracapacitors et al.), and 5) inverters dc−link capacitors. A virtual inertia control is proposed in [6] through an adjustable speed synchronous condenser, wherein a fuzzy controller governs the inertia power to prevent the diminution of inertial force in the power grid. Motivated by SG dynamics, the KHI scheme developed in [7] constructs governor unit and automatic voltage regulator on a digital control platform to generate phase and voltage references of a virtual synchronous machine. The references are then transformed to inverter current using algebraic phasor representation. Akin to SGs rotor, a huge amount of kinetic energy is preserved in the blades of wind turbines. However, in conventional variable speed wind turbines this energy does not contribute to frequency regulation unless ancillary control mechanisms are embedded in the interfaced converter control [8]. Ref. [9] equipped a doubly fed induction generator (DFIG)−based wind turbine with a dynamic frequency support control, composed of a de−loading pitch controller, an optimized maximum power point tracking (MPPT)

controller, and an adjustable frequency droop coefficient. Accordingly, the inertial response and primary frequency regulation are achieved. A variable proportion coefficient based controller is proposed in [10] for DFIG−based wind turbines aimed at frequency support by regulating rotor speed. First, the variable proportion coefficient is designed to provide virtual inertia. Then, a fuzzy controller is employed to design the variable proportion coefficient for quickly restoring the MPPT operation of DFIG−based wind turbine. Ref. [11] introduced a new distributed control for islanded photovoltaic−battery−hybrid systems; in which a PQ decoupling network enables controlling of individual converters using local measurements. And, the battery converter governed by a droop controller participates in regulating the islanded grid voltage and frequency. The distributed virtual inertia method in [12] uses the dc capacitors of grid−tied power converters as the energy buffer for frequency stability improvement. Therein, any frequency oscillation is linked to the dc voltage controller, allowing the dc−link voltage to fluctuate within permissible range. Accordingly, the energy provided by the capacitor is equivalent to the kinetic energy of SG rotor.

In this paper, a double−stage PV generator is augmented with a SIE to curb grid frequency fluctuations following supply−demand mismatches. The generator is controlled in voltage−oriented synchronous coordinate mode and a fast but accurate FLL synchronizes the generator with the host grid. Moreover, the inertia power is provided by an ultracapacitor employed in the dc link. The rest of paper is organized as follows: Section II describes the system structure. The control scheme is then introduced in Section III. Section IV presents the small−signal state−space realization of the system. The efficacy of the controller is validated by simulations in Section V. The paper ends with conclusions in Section VI.

II. System Description

Throughout this work, the entire modeling and control methodology is implemented in synchronous coordinates; in which quantities are denoted by complex−valued space vectors. Furthermore, set points and internal control commands are marked with "$\star$" in superscripts.

The model of PV generator understudy is shown in Fig. 1, comprising a solar array, a boost converter, and an inverter. An LC filter is the interface between the PV generator and the host grid that smooths the inverter current $\boldsymbol{i}_w$. An ultracapacitor is employed as the energy buffer aimed at improving grid frequency stability during supply−demand mismatch. The controller operates in the point of interconnection (PoI) voltage−oriented synchronous coordinate, where $\boldsymbol{u}_p = u_{pd} + j0$. The PV array current i_{pv} and voltage u_{pv} are sensed to control the boost converter with MPPT algorithm. Also, the inverter regulates the power injection through the measured inverter current $\boldsymbol{i}_w$, PoI voltage $\boldsymbol{u}_p$, and dc−bus voltage u_{dc}.

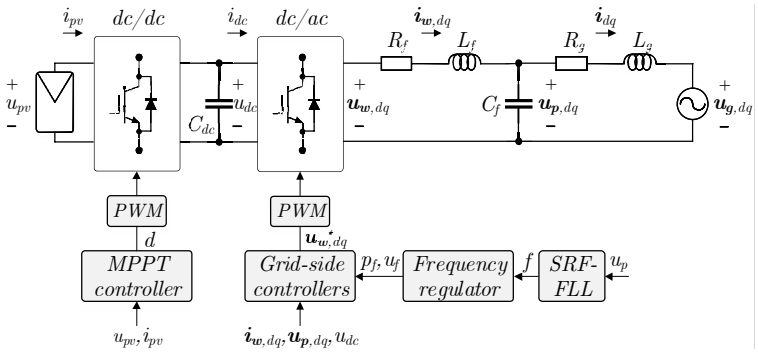

Fig. 1: PV generator model in the synchronous reference frame (SRF).

III. Control Methodology

A. DC−Side Converter

The diagram of front−end converter and MPPT controller is depicted in Fig. 2. The PV array model is:

$$u_{pv} = \frac{N_s n k T}{q} \ln\left(\frac{N_p I_{SC} - i_{pv}}{N_p I_0} + 1\right) \tag{1}$$

where quantities T, n, I_{SC}, and I_0 denote the junction temperature, the ideality factor, the short circuit current, and the saturation current of the PV cell, respectively. Also, k and q are Boltzmann and charge of the electron constant, and N_s (N_p) represents number of series (parallel) PV panels.

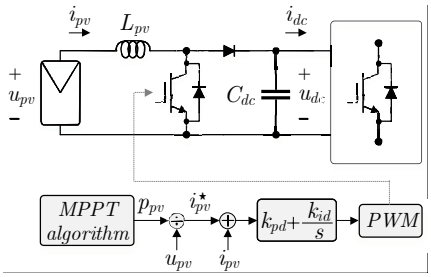

Fig. 2: Diagram of the dc/dc converter and the MPPT controller.

The MPPT control uses the error signal $i^{\star}_{pv} - i_{pv}$ to generate the converter duty cycle as:

$$d = k_{pd}\left(i^{\star}_{pv} - i_{pv}\right) + \underbrace{k_{id}\int\left(i^{\star}_{pv} - i_{pv}\right)dt}_{\varphi_d} \tag{2}$$

where $i^{\star}_{pv} = p_{pv}/u_{pv}$, and p_{pv} is the PV array output power. A step−up converter is employed to boost the PV array voltage to a proper level for the dc−link of inverter. The dc−bus voltage is also regulated at $u^{\star}_{dc}$ using the inverter control. Applying the state−space averaging method, the dynamics of the boost converter and the dc−link voltage are:

$$\dot{i}_{pv} = \frac{1}{L_{pv}}u_{pv} - \frac{1-d}{L_{pv}}u_{dc} \tag{3}$$

$$\dot{u}_{dc} = \frac{1-d}{C_{dc}}i_{pv} - \frac{1}{C_{dc}}i_{dc} \tag{4}$$

in which i_{dc} can be represented by the real power balance between ac− and dc− sides of the inverter as:

$$i_{dc} = \frac{\frac{3}{2}\left(u_{pd}i_{wd} + u_{pq}i_{wq}\right)}{u_{dc}}. \tag{5}$$

B. AC−Side Converter

The control strategy applied to the inverter comprises mainly four loops: 1) synchronization unit, 2) fast ac current control (ACC), 3) dc voltage control (DVC), 4) synthetic inertia emulator (SIE).

1. FLL Loop

To synchronize the inverter with the host grid, a SRF−FLL [13] is used here as it enjoys fast and accurate response, and improved filtering performance. The full structure of the employed synchronization unit is brought in Fig. 3. It acts as a nonlinear negative−feedback controller, driving the q−part of PoI voltage to zero. The state−space equation governing the SRF−FLL dynamics is obtained as:

$$\dot{\delta} = \omega = \omega_0 + \underbrace{\frac{k_{fll}d_{fll}}{u^2_{pd0}}\int(u_{pq}\widehat{u_{pd}} - u_{pd}\widehat{u_{pq}})dt}_{\varphi_\delta} + \frac{d_{fll}}{u_{pd0}}(u_{pq} - \widehat{u_{pq}}) \tag{6}$$

where $\widehat{u_{pd}}$ and $\widehat{u_{pq}}$ are the estimated d− and q− components of PoI voltage, respectively:

$$\dot{\widehat{u_{pd}}} = k_{fll}(u_{pd} - \widehat{u_{pd}}) \tag{7}$$

$$\dot{\widehat{u_{pq}}} = k_{fll}(u_{pq} - \widehat{u_{pq}}). \tag{8}$$

The operating principle and parameters design of the SRF−FLL can be found in [13].

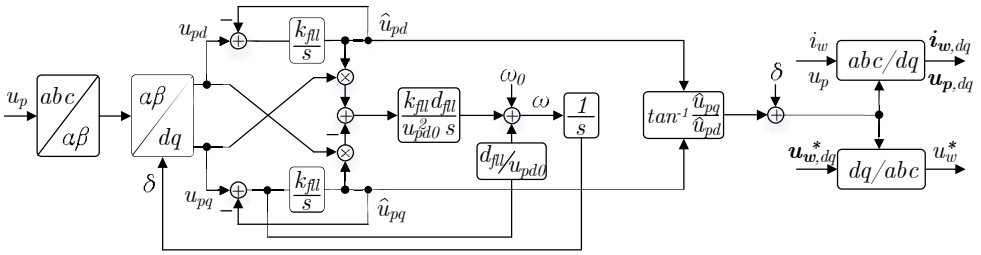

Fig. 3: FLL structure.

2. ACC Loop

The ACC governs the inverter current to its nominal $\boldsymbol{i}^{\star}_{w}$ by a proportional−integral (PI) controller. The PoI voltage feedforward, cancellation of the dq−cross coupling, and active resistance terms are also considered in the ACC for better dynamic performance (cf. Fig. 4). The voltage reference $\boldsymbol{u}^{\star}_{w}$ to pulse−width modulation (PWM) block is then formed as:

$$\boldsymbol{u}^{\star}_{w} = \boldsymbol{u}_p + j\omega L_f \boldsymbol{i}_w - r\boldsymbol{i}_w + k_{pi}(\boldsymbol{i}^{\star}_{w} - \boldsymbol{i}_w) + \underbrace{k_{ii}\int(\boldsymbol{i}^{\star}_{w} - \boldsymbol{i}_w)dt}_{\varphi_{i_{w,dq}}}. \tag{9}$$

The d−axis current reference $i^{\star}_{wd} = 2p^{\star}_{w}/3u_{pd0}$ is determined by two terms; 1) DVC output or p_u, and 2) SIE output or p_f which are described in following subsections. Also, the reactive power requirement defines $i^{\star}_{wq} = -2q^{\star}_{w}/3u_{pd0}$. Using the algorithm given in [14], k_{pi}, k_{ii} and r are set to $\alpha_i L_f$, $\alpha_i^2 L_f$, and $\alpha_i L_f$, respectively; in which α_i is the ACC bandwidth.

3. DVC Loop

The DVC maintains the dc−link voltage at its reference $u^{\star}_{dc}$ in steady state condition. It operates on the error $[u_{dc}^2 - (u^{\star}_{dc} - u_f)^2]/2$ by a PI controller, in which the signal u_f manipulates the dc−link voltage reference during frequency disturbance; so as the ultracapacitor C_{dc} provides synthetic inertia power for the grid. The term u_f is later defined with frequency regulator. The PI parameters correspond to the DVC are selected based on the method in [15], i.e. $k_{pu} = \alpha_u C_{dc}$ with a small k_{iu}. And, α_u is the DVC bandwidth so that $\alpha_u \leq 0.1\alpha_i$; because, as a general rule, the outer controller must be slower than the inner controller. Thus, p_u is obtained as:

$$p_u = k_{pu}\frac{\left[u_{dc}^2 - (u^{\star}_{dc} - u_f)^2\right]}{2} + \underbrace{k_{iu}\int\frac{\left[u_{dc}^2 - (u^{\star}_{dc} - u_f)^2\right]}{2}dt}_{\varphi_u}. \tag{10}$$

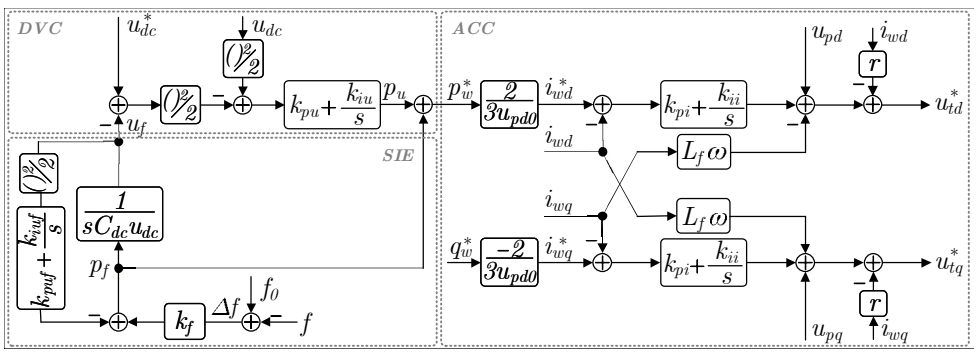

Fig. 4: Inverter controller configuration.

4. SIE Loop

It manipulates $u^{\star}_{dc}$ so as the inverter injects (absorbs) inertia power when the grid frequency falls (rises). This energy is supplied (stored) by the dc−bus ultracapacitor. To this end, the measured frequency oscillation Δf is linked to p_f through the synthetic inertia gain k_f. The inverter hence can provide p_f if the ultracapacitor voltage declines (increases) by:

$$u_f = \int \frac{p_f}{C_{dc} u_{dc}} dt. \tag{11}$$

The new dc−link voltage reference is then $u^{\star}_{dc} \mp u_f$ (minus and plus are for step−up and step−down changes in the demand, respectively). The ancillary signal u_f must reach zero (by a PI controller as shown in Fig. 4) within a certain time after the frequency disturbance; otherwise, the ultracapacitor voltage drifts with the time from its nominal. It is worth noting that k_{puf} and k_{iuf} defines dc voltage recovery time (higher values yield shorter time). The frequency regulator output is then revised as:

$$p_f = k_f \Delta f - k_{puf} \frac{u_f^2}{2} - \underbrace{k_{iuf} \int \frac{u_f^2}{2} dt}_{\varphi_{uf}}. \tag{12}$$

IV. Small−Signal Stability Analysis

This section appraises the impact of parameters C_{dc}, k_f, and SRF−FLL controller gains on the generator stability. The analysis is based on eigenvalues; accordingly, the linearized state−space model (evaluated at an specific operating point) is extracted as the standard form of:

$$\Delta \dot{x} = \mathbf{A} \Delta x + \mathbf{B} \Delta u \tag{13}$$

in which the state vector x and the input vector u are selected, respectively:

$$x = [\delta \; \varphi_\delta \; i_{wd} \; i_{wq} \; u_{pd} \; u_{pq} \; \widehat{u_{pd}} \; \widehat{u_{pq}} \; i_{pv} \; u_{dc} \; \varphi_d \; u_f \; \varphi_{uf} \; \varphi_u \; \varphi_{i_{wd}} \; \varphi_{i_{wq}} \; i_d \; i_q]^T_{1\times 18} \tag{14}$$

$$u = [p_{pv} \; q^{\star}_w]^T_{1\times 2}. \tag{15}$$

Table I: PARAMETERS OF THE PV GENERATOR AND THE GRID

Parameter	Value	Parameter	Value
R_f, R_g	0.1 Ω, 0.1 Ω	k_f	4000
L_f, L_g	2.94 mH, 2 mH	α_i	2π.400 rad/s
C_f, C_{dc}	10 μF, 1 F	α_u	2π.40 rad/s
ω_0	2π.50 rad/s	k_{pd}, k_{id}	0.3, 20
$u^{\star}_p$, $u^{\star}_{dc}$	$\sqrt{2/3}$.400 V, 750 V	k_{fll}, d_{fll}	40π, 40π
p_{pv}, $q^{\star}_w$	20 kW, 0 kVAr	k_{puf}, k_{iuf}	1, 0.001

The specifications of the PV generator understudy are presented in Table I. We first study the impact of ultracapacitor on the generator stability. With higher dc−link capacitor, more inertia emulation can be achieved. The dominant poles of the system is shown in Fig. 5(a), where C_{dc} is increased by multiplying $1 \leq \beta_{Cdc} \leq 10$. As observed from this figure, the poles are hardly sensitive to the change of C_{dc}. The generator remains stable as no pole moves toward the right−side of the s−plane. Thus, the dc−side capacitance can be enlarged aimed at providing more supplementary power during supply−demand mismatch. The effect of synthetic inertia gain k_f on system eigenvalues is illustrated in Fig. 5(b). Again, more synthetic inertia power is provided by increasing k_f; which further improves the frequency stability indices. However, the eigenvalue analysis shown in Fig. 5(b) reveals that the control system is prone to become unstable for high values of k_f (> 4000) as the mode 10 moves to the right−half s−plane. Fig.

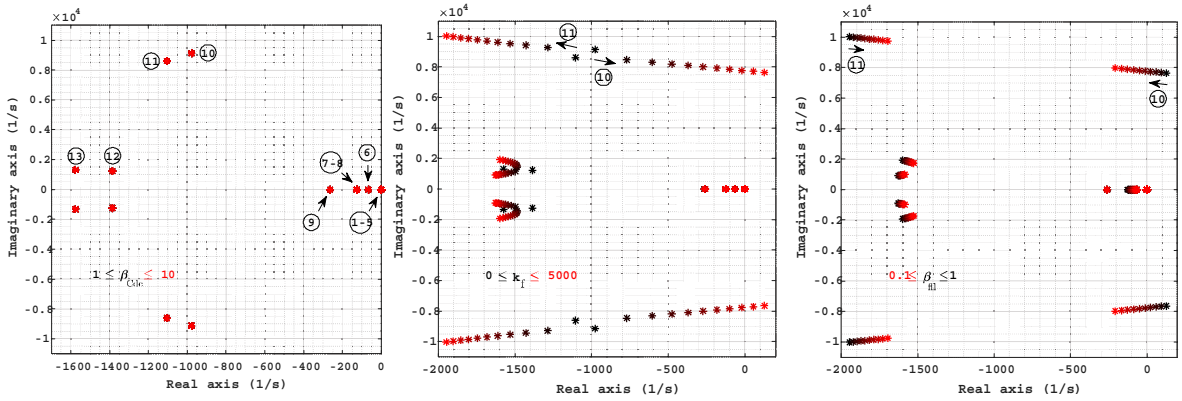

(a) (b) (c)

Fig. 5: Effect of a) C_{dc}, b) k_f, and c) SRF−FLL controller gains on the pole diagram.

5(c) depicts the system pole diagram as the SRF−FLL controller gains are decreased by multiplying $0.1 \leq \beta_{fll} \leq 1$ (i.e. $k_{fll} = d_{fll} = 40\pi \rightarrow 4\pi$). The eigenvalue interpretation demonstrates that reducing the SRF−FLL bandwidth can stabilize the control system for high k_f; but, it yields slower grid frequency tracking. Consequently, the responsiveness of SIE loop in enhancing frequency stability metrics is limited as we will show in Section V.

V. Simulation Results

This section includes the average−model based simulations of the PV generator in MATLAB/Simulink. The interfaced inverter operates under following conditions: the rated power is 20 kVA and the operating voltage is 400 V. The capacitor voltage is expected to stay within $700 \leq u_{dc} \leq 800$ V for 2 kW inertia power. Also, ∓ 0.5 Hz step−changes in the grid frequency are considered as the worst−case input disturbances. Other parameters of the system are set as Table I.

Fig. 6 depicts the SRF−FLL response in terms of different k_{fll} and d_{fll}. As observed, perfect grid synchronization is attained within less than 0.4 s. Tracking the grid frequency occurs slower as the SRF−FLL bandwidth decreases. Hence, it limits the responsiveness of SIE as we will illustrate in Fig. 8. The PV generator power is shown in Fig. 7. Following the defined frequency disturbances, the inverter augmented with SIE ($k_f = 4000$) provides 2 kW inertia power to curb the frequency stability indices. The additional power is equivalent to the released or absorbed kinetic energy by SGs after the supply−demand mismatch. As stated earlier, higher k_f yields better frequency dynamics; however, it

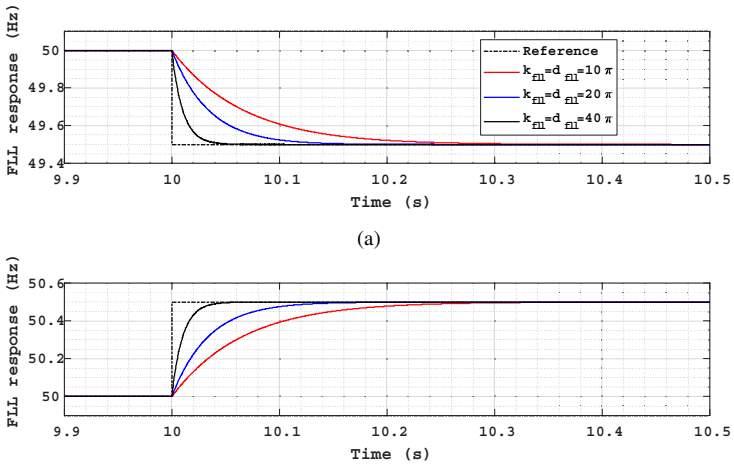

(a)

(b)

Fig. 6: SRF−FLL response for a) step−down and b) step−up change in the grid frequency.

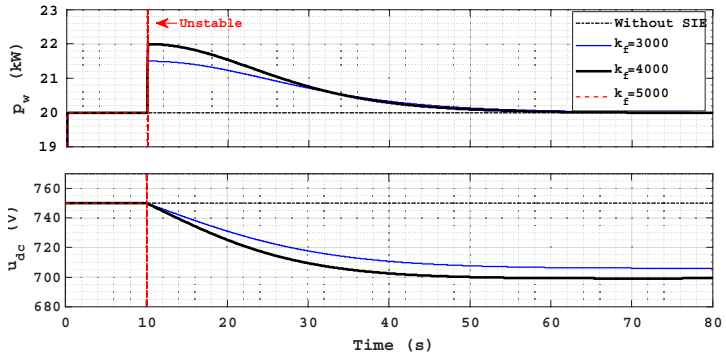

(a)

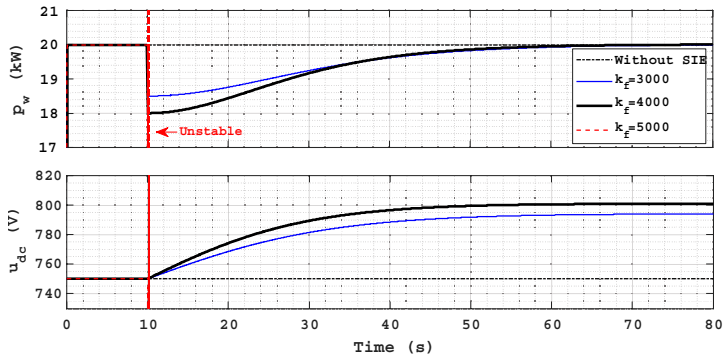

(b)

Fig. 7: Inverter outputs (active power and dc−bus voltage) for a) step−down and b) step−up change in the grid frequency.

induces instability to the controller. It is vindicated because high k_f shifts a local mode of the controller toward the right−half s−plane [cf. Fig. 5(b)]. Fig. 7 also demonstrates the dc capacitor voltage. The capacitor acts as the energy buffer; Thus, it starts discharging or charging after the disturbances. It should be emphasized that the dc voltage remains in the permissible range.

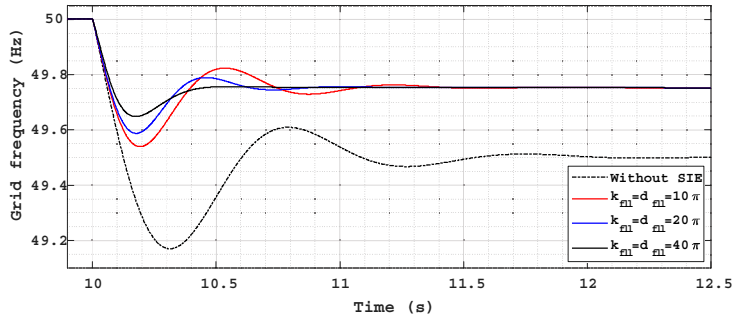

(a)

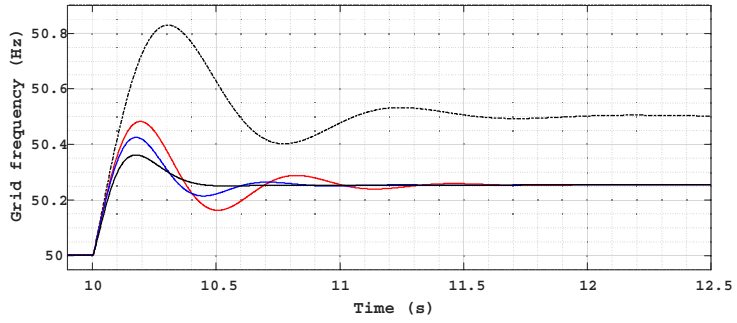

(b)

Fig. 8: Grid frequency measured at the PoI following a) step−up and b) step−down change in the demand.

Next, the frequency dynamics of the grid with and without SIE are studied. To this end, a 20 kVA SG models the host grid. The governor with droop characteristic of 5%, and IEEE type AC5A excitation system regulate the SG mechanical input and field voltage, respectively. The SG in cooperation with the PV generator supplies power to a local load of 40 kW. Again, $\pm 10\%$ sudden changes in the local load are considered as the input disturbances. Fig. 8 shows the measured frequency variations at the point of common coupling. It is clear that the SIE can effectively enhance the frequency nadir and RoCoF metrics. Also, using SRF−FLL with smaller bandwidth limits the effectiveness of frequency regulator. For example, with $k_{fll} = d_{fll} = 40\pi$, the frequency nadir and the RoCoF are improved by 1% and 20%, respectively compared to the case in which the SIE is deactivated. These values are decreased to 0.73% and 6.67%, respectively for $k_{fll} = d_{fll} = 10\pi$.

VI. Conclusion

Herein, we scrutinized the impact of SIE and SRF−FLL bandwidth on the stability of a double−stage PV generator. Eigenvalue analyses revealed that high synthetic inertia gains (aimed at providing better frequency support) induce instability to the inverter controller. This problem can be solved by reducing the FLL bandwidth; however, it considerably limits the responsiveness of the SIE in enhancing frequency stability metrics. As an interesting topic for future works, the instability problem of such generators in high SIE gains could be addressed by ancillary compensators embedded in the inverter controller. Accordingly, more synthetic inertia power could be provided by the generator while the system remains stable.

References

[1] Saeedian M., et al.: Emulating Rotational Inertia of Synchronous Machines by a New Control Technique in Grid-Interactive Converters, Sustainability Vol. 12 no. 13, pp. 5346-5360

[2] Løvengreen S., and Mancarella P.: Mapping the Frequency Response Adequacy of the Australian National Electricity Market, AUPEC 2017, pp. 1-6

[3] Saeedian M., et al.: A Control Technique Based on Distributed Virtual Inertia for High Penetration of Renewable Energies Under Weak Grid Conditions, IEEE Systems Journal Vol. 15 no. 2, pp. 1825-1834

[4] Stanojev O., et al.: MPC-Based Fast Frequency Control of Voltage Source Converters in Low-Inertia Power Systems, IEEE Trans. Power Systems, doi: 10.1109/TPWRS.2020.2999652

[5] Chen T., Guo J., Chaudhuri B., and Hui S. Y.: Virtual Inertia From Smart Loads, IEEE Trans. Smart Grid Vol. 11 no. 5, pp. 4311-4320

[6] Matsuda K., et al.: Stabilization of Power System by Virtual Inertia Control of Adjustable Speed Synchronous Condenser, ICREST 2021, pp. 163-167

[7] Hirase Y., Abe K., Sugimoto K., and Shindo Y.: A Grid-Connected Inverter with Virtual Synchronous Generator Model of Algebraic Type, Electrical Engineering in Japan Vol. 184 no. 4, pp. 11-21

[8] Saeedian M., Pournazarian B., Taheri S., and Pouresmaeil E.: Provision of Synthetic Inertia Support for Converter-Dominated Weak Grids, IEEE Systems Journal, doi: 10.1109/JSYST.2021.3060866

[9] Fu Y., Wang Y., and Zhang X.: Integrated Wind Turbine Controller with Virtual Inertia and Primary Frequency Responses for Grid Dynamic Frequency Support, IET Renewable Power Generation Vol. 11 no. 8, pp. 1129–1137

[10] Peng X., et al.: Two-Stage Variable Proportion Coefficient Based Frequency Support of Grid-Connected DFIG-WTs, IEEE Trans. Power Systems Vol. 35 no. 2, pp. 962-974

[11] Pan Y., Sangwongwanich A., Yang Y. G., and Blaabjerg F. G.: Distributed Control of Islanded Series PV-Battery-Hybrid Systems with Low Communication Burden, IEEE Trans. Power Electron., doi: 10.1109/TPEL.2021.3063111

[12] Saeedian M., et al.: Grid-Following DVI-Based Converter Operating in Weak Grids for Enhancing Frequency Stability, IEEE Trans. Power Delivery, doi: 10.1109/TPWRD.2021.3059898

[13] Quan X., et al.: A Novel Synchronous Reference Frame Frequency-Locked Loop, arXiv preprint arXiv:1908.08669

[14] Harnefors L., Zhang L., and Bongiorno M.: Frequency-Domain Passivity-Based Current Controller Design, IET Power Electron. Vol. 1 no. 4, pp. 455-465

[15] Harnefors L., Bongiorno M., and Lundberg S.: Input-Admittance Calculation and Shaping for Controlled Voltage-Source Converters, IEEE Trans. Ind. Electron. Vol. 54 no. 6, pp. 3323-3334